Utah State University

DigitalCommons@USU

All Graduate Plan B and other Reports

Graduate Studies

5-2012

Investigation of Relative Importance of Some Error Sources in Particle Image Velocimetry

Jeff R. Harris
Utah State University

Follow this and additional works at: https://digitalcommons.usu.edu/gradreports

Part of the Mechanical Engineering Commons

Utah State University
MERRILL-CAZIER LIBRARY

INVESTIGATION OF RELATIVE IMPORTANCE OF SOME ERROR SOURCES

IN PARTICLE IMAGE VELOCIMETRY

by

Jeff R. Harris

A report submitted in partial fulfillment
of the requirements for the degree

of

MASTER OF SCIENCE

in

Mechanical Engineering

Approved:

_____   _____
Dr. Barton Smith   Dr. Robert E. Spall
Major Professor   Committee Member

_____
Dr. Heng Ban
Committee Member

UTAH STATE UNIVERSITY
Logan, Utah

2012

Abstract

Investigation of Relative Importance of Some Error Sources in Particle Image Velocimetry

by

Jeff R. Harris, Master of Science

Utah State University, 2012

Major Professor: Dr. Barton Smith
Department: Mechanical and Aerospace Engineering

Many factors contribute to uncertainty in particle image velocimetry (PIV) measurements. The objective of this report is to investigate some commonly cited uncertainty sources and to show means that can be used to quantify the error sources. These error sources are: magnification, calibration, perspective, resolution and the correlation algorithm. Experiments were conducted to quantify the impact these factors have on PIV velocity measurements. Several methods are presented to demonstrate how to measure the uncertainty or error for a PIV experiment. Some error quantities are computed and found experimentally. Several error sources (such as magnification and calibration) were found to be insignificant for most experimental setups. Some sources depend highly on the experimental setup, and should be computed for every experiment. One method that has been presented for finding the algorithm "noise floor" was found to be unreliable for small particle image sizes.

(64 pages)

Public Abstract

Investigation of Relative Importance of Some Error Sources in Particle Image Velocimetry

Jeff R. Harris

Particle image velocimetry (PIV) is an optical technique used to measure fluid velocity. PIV measurements have many sources that create uncertainty in the velocity results. The objective of this report is to investigate some commonly cited uncertainty sources and to show methods than can be used to find the value of the uncertainty sources. These sources are: magnification, calibration, perspective, resolution and the computation scheme. Experiments were conducted to find the impact that sources have on the velocity measurements. Several methods are presented to demonstrate how to measure the uncertainty of error for a PIV experiment. Some error quantities are computed and found experimentally. Several error sources were found to be small. Some sources depend on the setup of the experiment and should be computed for every experiment. One method that has been presented for finding the uncertainty in the computation scheme was found to be unreliable for small particles.

To those who to struggle with Math...

Acknowledgments

Thanks to Dr. Smith, Brandon Wilson, Kyle Jones, INL and the DoE. I'd be filled with uncertainty without your help.

Jeff R. Harris

Contents

List of Tables

List of Figures

Notation

d_τ particle image diameter

M_0 magnification (z_i/Z_o)

S_x standard deviation in the x direction

u' standard deviation of a velocity vector

$u'u'$ RMS of u velocity reported from DaVis 7.2

Z_o distance from lens to object plane

z_i distance from lens to image plane

Δx displacment in the x direction

Δy displacment in the y direction

Δz displacment in the z direction (out of plane motion)

Δz_0 laser sheet thickness

ϵ perspective error vector

θ_x projection of the viewing angle on the x-z plane

θ_y projection of the viewing angle on the y-z plane

σ standard deviation of the correlation fit

Acronyms

CFD   Computational Fluid Dynamics

FFT   Fast Fourier Transform

PIV   Particle Image Velocimetry

Chapter 1

Introduction

Particle Image Velocimetry (PIV) is an experimental method used to measure fluid velocity fields. Experiments that use PIV to measure fluid flow inherently have many sources of uncertainty in the measurement. Several of these sources are analyzed and their significance is examined. Some of the uncertainty sources are compared with conclusions in Adrian and Westerweel [1]. Methods for quantifying errors are also presented.

The error sources that were chosen to be analyzed were based on conclusions (or lack thereof) made by Adrian and Westerweel [1]. Raffel, Willert and Kompenhans [2] also discuss several sources of error. Their conclusions were used to confirm results in this report. Many ideas were presented at The Particle Image Velocimetry Uncertainty Workshop [3]. Some of the presentations included experimental or numerical means to quantify the error sources. Some of those methods were used and conclusions were made about their accuracy. The objectives of this report include the following:

- From the discussion in the works cited above, several PIV uncertainty sources were chosen for analysis.

- Analysis of the sources were completed using analytical or numerical means of quantification.

- These results were tested using experimental quantification for analytical confirmation.

- The means used to quantify the uncertainty (both numerically and experimentally) are included.

1.1 Motivation

In many industries where fluid flow and heat transfer are important, computational fluid dynamics (CFD) is a major tool for design and operational safety. CFD algorithms compute fluid flow using numerical approximations of mathematical turbulence models. The accuracy of the fluid flow approximation from CFD is based on the numerical approximation used and the flow conditions, *i.e.*, geometry, boundary conditions, fluid properties, etc. Different flow scenarios require different turbulence models.

To increase trust in a CFD approximation, many industries turn to experiments to measure a feature of the fluid flow (velocity, pressure, etc.). The experimental results are then compared with a CFD simulation of the same experiment. In order for the comparison to be useful, the uncertainty of the experimental data and the CFD simulation should be shown. One difficult task in this simulation validation is calculating the uncertainty of the experimental data. PIV uncertainty is not fully understood to date, and this report simply shows several potential uncertainty and error sources and how to quantify them.

1.2 Particle Image Velocimetry

This section discusses the fundamentals of particle image velocimetry. Previous studies on the accuracy of the method are cited.

1.2.1 Fundamentals

Particle Image Velocimetry is an optical fluid velocity measurement technique. It is a non-obtrusive means to obtain velocity data on a plane in the fluid. Before PIV, probes (such as hot wires or pitot probes) were inserted into the flow. These probes create obstructions and alter the flow, increasing uncertainty in the measurements. PIV methods do not obstruct the flow, so the flow characteristics remain unaltered. The non-obtrusive nature of the method gives many advantages over using probes.

Laser speckle velocimetry can be considered the predecessor to particle image velocimetry. PIV images were originally acquired using film, which had many shortcomings compared to the digital methods used today [4]. With improvements in computing power and digital

cameras, the measurement technique became digital. Early analysis of the digital method provided guidance for the development of the hardware and software that is currently used. The work done by Nashino pushed the move to use digital cameras by presenting turbulence statistics that were previously unattainable when measuring with film PIV [5]. Prasad, Adrian, Landreth, and Offutt discuss the imaging of particles using various resolutions of imaging arrays on the digital cameras [6]. The auto-correlation method (which was used before the study in [7]) was eventually replaced with the cross-correlation technique that is used today [7]. For a more thorough historical summary, see [8].

The general scheme of a PIV experiment includes building a flow facility with transparent walls and using a fluid that is optically clear. The fluid is combined with small particles called "seed." For the experiments in this project, the fluid was air and olive oil droplets were mixed into the air for seed.

The seed in the fluid is illuminated by a laser sheet (a laser beam that is converted to a laser plane using a cylindrical lens). The laser sheet acts like a camera flash while a camera takes images of the particles in the flow. The timing of the laser and camera is crucial to obtaining quality PIV data. Using a cross-correlation algorithm, the displacement of the particles in small sections (referred to as interrogation regions) of the image is computed. The distance the particles move and the time between the images provides a velocity vector for each interrogation region of the image.

The setup for this project includes two jets that have a nearly identical PIV setup. The first jet is laminar upstream of the exit and PIV data is acquired near the exit of the jet. The second jet is turbulent with the PIV data also taken near the jet exit. Hot wire measurements were also acquired with the PIV data. Unless otherwise noted, the PIV data came from the turbulent jet.

In much of the discussion, it is first necessary to understand how particle position impacts the velocity measurement. Since the difference in the mean position of a particle in two images is used to find a displacement, which is then divided by the time between the images to obtain a velocity, an error in the two positions results in displacement error

and thus a velocity error. Also, velocity and position are usually reported in pixels in this report. Pixel displacement is multiplied by a scale factor to get a spatial displacement (in units of mm), and divided by the time between the images to get a velocity. Thus, pixel displacement is velocity.

1.2.2 Accuracy

Raffel, Willert and Kompenhans [2] discuss the optimization of particle image diameter. It was found that the optimal particle image diameter to minimize the RMS uncertainty was 2 pixels. Also discussed is the optimization of particle image shift, the effect of particle image density, background noise, displacement gradients and out-of-plane motion is merely mentioned.

Bolinder found that shifting the interrogation windows increased the accuracy of the correlation method [9]. The post-processing of the velocity results is discussed by Nogueira, Lecuona and Rodriguez, where removing spurious vectors was found to increase the accuracy of the method [10]. It is now common practice to remove bad vectors from the correlation results, using detection algorithms as discussed by Westerweel [11].

Adrian and Westerweel also discuss several parameters of PIV accuracy in [1]. Tracer dynamics, which is also referred to as slip error, and image mapping (magnification and perspective) are included in that discussion. Not much is stated about the contribution of the error sources to velocity error, however.

1.3 Uncertainty

Uncertainty is an estimate of how far a measurement could be from the true quantity with some level of confidence (usually 95%, [12]). Coleman and Steele [13, p. 5]suggest that the uncertainty "interval is an estimate of a range within which we believe the actual (but unknown) value of an error lies."

Two types of uncertainty are included in the present study, systematic and random. Systematic uncertainty is a fixed uncertainty stemming from the measurement equipment. Random uncertainty comes from inconsistencies in repeated data acquisition, and can often

be minimized by increasing the number of data points. The complex nature of PIV measurements creates a large pool of possible uncertainty sources. The error sources chosen here are those mentioned by Adrian [1] or at the PIV Uncertainty Workshop [3]. These sources can be addressed using equipment and software available in the Experimental Fluid Dynamics Laboratory at USU. The sources that are considered in the present work are listed below and these sources are later discussed in more depth, along with the findings from each analysis.

1. Magnification: Uncertainty introduced from the variation of the magnification of the particle images.

2. Calibration: Uncertainty introduced from the calibration method.

3. Perspective Error: Uncertainty introduced from the lens perspective and out of plane motion.

4. Resolution: The error introduced by spatially averaging turbulent fluctuations.

5. Algorithm: Uncertainty introduced from the correlation method.

Chapter 2

Equipment

2.1 Flow Apparatus

Fig. 2.1 shows a schematic of the turbulent jet that was used to collect data. The flow was driven by a frequency controlled blower upstream, pushing air into a flow conditioner then into the contraction and exiting as a rectangular jet. The air was seeded at the blower outlet with olive oil. This jet was chosen because of its high turbulence level.

The turbulence kinetic energy was found for the jet using the isotropic turbulence approximation. This approximation assumes that the fluctuations in v and w (where the jet velocity is in the u direction, and w is normal to the laser plane) are of similar magnitudes. To confirm the isotropic turbulence approximation, a PIV data set was taken to obtain the u and w components of velocity. In the center of the jet, the out of plane fluctuation levels were found to be within 1.5% of the in-plane v fluctuation levels.
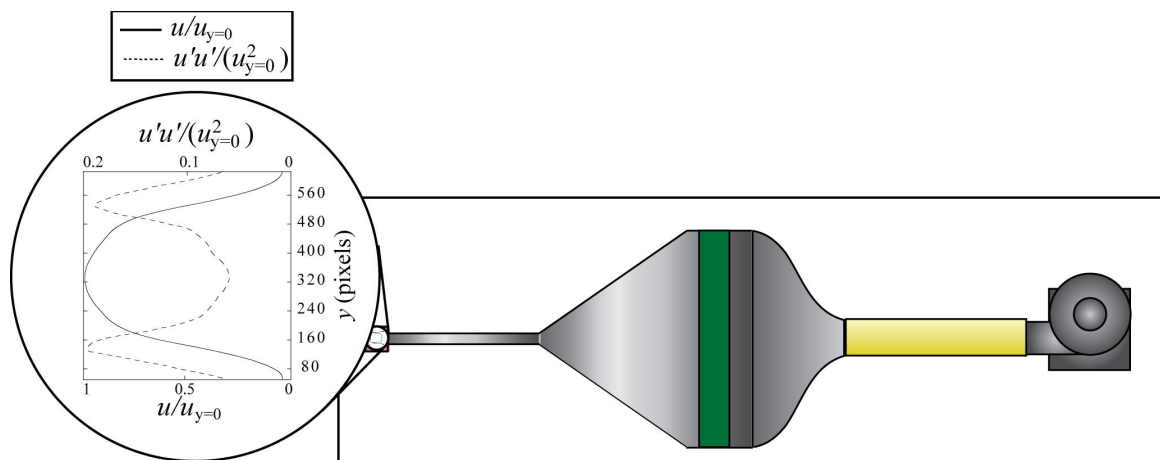
Fig. 2.1: A schematic of the jet flow apparatus.

2.2   PIV Equipment

PIV requires at least one camera and a laser. The camera for this project is the Imager Intense camera from the LaVision Flowmaster PIV system. It has a 12 bit imaging chip with a pixel size of 6.45 μm square. The chip is 1376 pixels×1040 pixels and can record at 10 frames/s. The laser is a Nd:YAG dual cavity laser that can fire 2 pulses at 50 mJ/pulse and 532 nm. This system was used to acquire the PIV data. A second, high-speed laser was used in the laser sheet thickness measurement, which is described below. The high speed laser is an Nd:YLF single cavity solid state laser capable of a 10 kHz repetition. The burst from the single head is 40mJ/pulse at 1 kHz repetition and has a 527 nm wavelength when being used for data collection.

When acquiring data in the jet, the laser was set above the jet and fired the light sheet down through the jet with the sheet aligned with the jet flow. The camera was positioned normal to the laser sheet, as shown in Fig. 2.2. The camera was fixed to a traverse stage for precise movement away from or closer to the laser plane. This expedited lens swapping and changing the field of view.

2.3   Laser Sheet Thickness

To quantify the error from the magnification variation and the perspective error, an accurate measurement of the laser sheet is needed. The laser sheet thickness was measured using two methods. The first was using laser burn paper, which is similar to photographic film in that it changes color when exposed to intense light. In a laser sheet, the black burn paper would turn white along the most intense part of the laser sheet, and decrease in whiteness as position is moved away from the intense section. The paper used was ZAP-IT® Laser Alignment Paper from Kentek®.

The paper was fixed in a position close to the area of interest when recording PIV data. The laser was fired until the paper was exposed to a desirable level. This method proved unreliable for the high speed laser because of difficulty controlling the power output. At high frequencies the laser would burn through the paper; at low frequencies, the laser never exposed the paper. A frequency that was "just right" was never found. The low speed laser
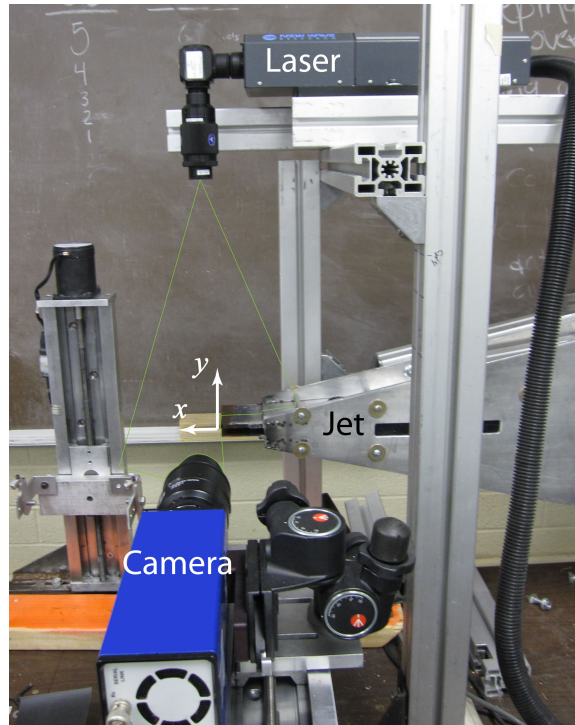
Fig. 2.2: The camera and laser positions for the jet flow.

was much easier to use with the burn paper, as it had a higher intensity output with each burst. The number of bursts was easily controlled and the exposure of the burn paper was more reliable.

The burn paper was then scanned and run through an algorithm that would fit the exposure intensity profile to a Gaussian or other matching curve. From that curve (which represented the intensity profile), a width of the laser sheet could be obtained.

Additionally, an instrument was built to measure an intensity profile using the photo-transistor. The eye of the sensor was taped over with black tape with a measured pinhole in the tape. Two razor blade shutters were put in front of the pinhole.

The pinhole was used to protect the sensor from overexposure, and the shutters made it possible to sample the laser sheet profile. The apparatus was traversed at very small increments through the laser sheet (0.2 mm steps). The space between the shutters was smaller than the incremental step size. Fig. 2.3 shows the instrument built to measure the laser sheet thickness.
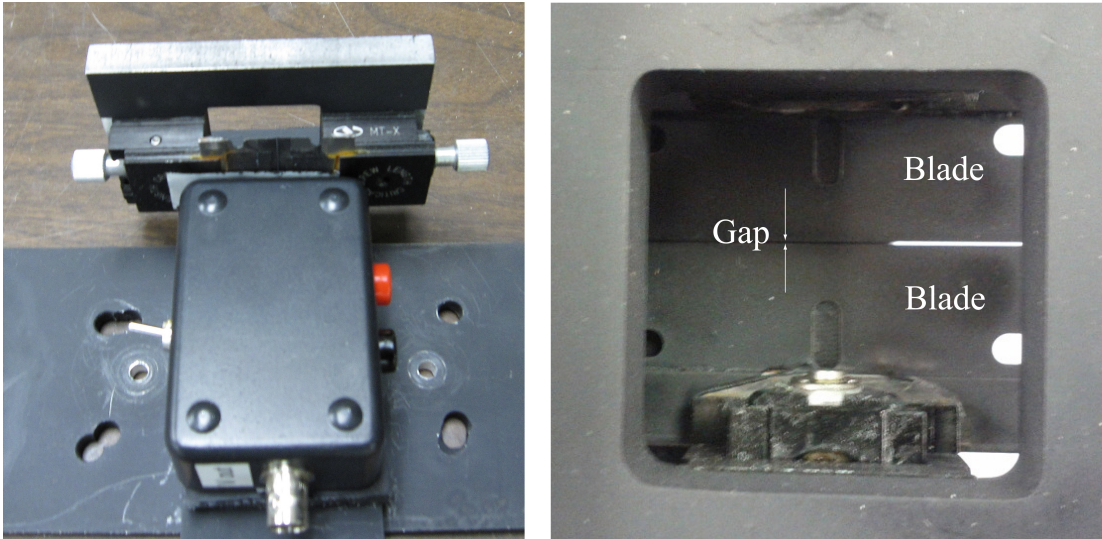
Fig. 2.3: The photo-transistor setup, with the shutters at the top of the image (left). Looking at the front of the sensor (right), the small space between the razor blades is shown. The laser sheet would be aligned with the space between the razor blades.

In Fig. 2.3, the laser sheet would be coming in from the top of the image on the left and into the page with the image on the right. The light sheet would go between the razor blades and hit the piece of tape with a pinhole. Then the light would illuminate the photo-transistor and the intensity was measured. The measured profile was then used to compute a laser sheet width.

Fig. 2.4 shows the circuit diagram for the sensor. The circuit was built to measure the intensity profile of a laser sheet, which requires the 10,000 ohm resistor. A switch was added that allows the circuit to be switched to a 10 ohm resistor for a step intensity measurement.

2.4 Hot-wire Anemometer

The hot-wire probe was used to measure the jet exit velocity. The hot wire does not have the same optical error sources that exist in PIV measurements, making hot-wire a good comparison for PIV measurements. Fig. 2.5 shows the placement of the probe relative to the jet exit. The probe was traversed across the jet exit plane in steps of 0.2 mm. The wire was aligned with the z axis in Fig. 2.5 to measure the main flow velocity and fluctuations in the y direction. The hot-wire was then rotated $90°$ and positioned in the center of the
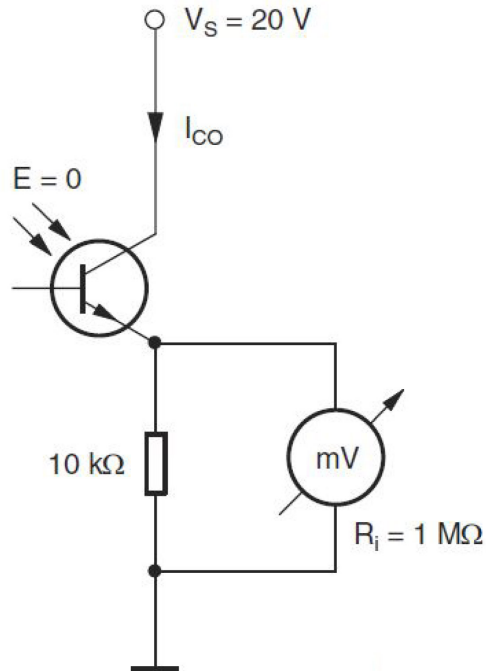
Fig. 2.4: The circuit diagram for the phototransistor.

jet to measure the main flow velocity and the fluctuations in the z direction.

The hot-wire anemometer was the IFA 100, and was calibrated before data acquisition using a controlled air flow and a TSI calibrator. Fig. 2.6 shows the calibration curve and the fit parameters for the curve. The fit parameters were used in the data acquisition to convert the probe voltage to velocity. A polynomial fit of order 3 was used for the curve fit.
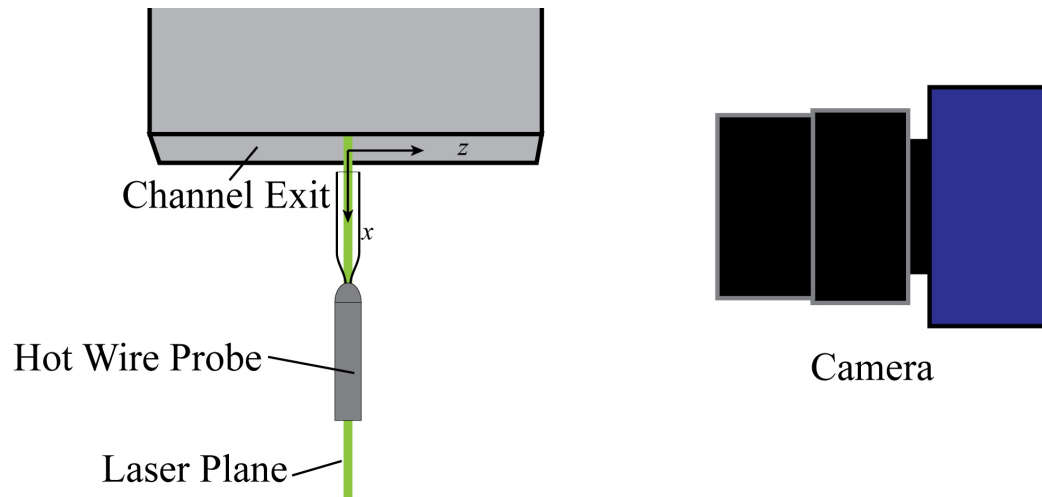
Fig. 2.5: A schematic of the jet flow apparatus, showing the camera and hot wire probe.

$$Y = M0 + M1*x + ... M8*x^8 + M9*x^9$$

M0	2.91
M1	3.909
M2	1.787
M3	0.31777
R	1
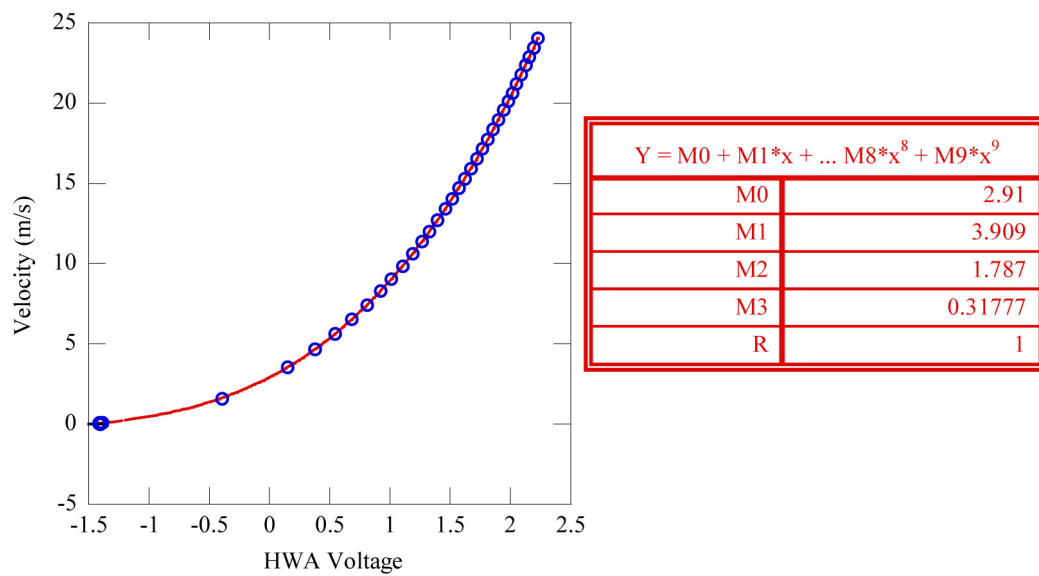
Fig. 2.6: A calibration for the hot wire probe. The curve fit coefficients are shown along with the data points, shown by the symbols and the curve fit is the line.

Chapter 3

PIV Uncertainty Sources

There are many sources that contribute to PIV uncertainty. Several of the sources are discussed along with the respective analysis. These sources were chosen based on previous discussion.

3.1   Magnification

The velocity resulting from PIV data is based on using a camera with a lens to obtain the desired field-of-view. The magnification of the image is used to convert the pixel position on the imaging chip to a physical distance in real space (on the object plane). When the object being viewed is not on the plane that the magnification was calibrated for, an error in the reported position of that object results. In PIV, a particle that is on the same plane as the calibration plane has no magnification error. However, a particle that is on the far side of the laser sheet (relative to the camera) is reported in a position that is in error.

The definition of magnification is shown in Eq. 3.1, where z_i is the distance from the lens to the image and Z_o is the distance from the lens to the object. When the particle is on the far side of the laser sheet, the object distance from the lens is increased by half of the laser sheet thickness (assuming the calibration is for the center of the laser sheet). This changes the magnification for particles on that plane. A relative difference of the magnification on the back plane compared with the center of the plane provides an error that is proportional to the laser sheet thickness (Δz_0) divided by the object distance. This error in magnification (being relative) can be directly applied to error on position. For most experiments, the relative difference of the magnification is 0.3% [1].

$$M_0 = z_i/Z_o \tag{3.1}$$

Fig. 3.1 shows the layout of the laser plane, lens plane and image plane. In the laser sheet, there are two particle positions shown. Position 1 shows a particle in the center of the laser sheet. This position is $\mathbf{x} = (x, y, 0)$. For position 2 in Fig. 3.1, the position of the particle is $\mathbf{x} = (x + \Delta x, y + \Delta y, \Delta z)$, but Δx and Δy are zero for this case. The angle between the z axis and the optical ray is referred to as θ_x, which will be discussed in more detail later.
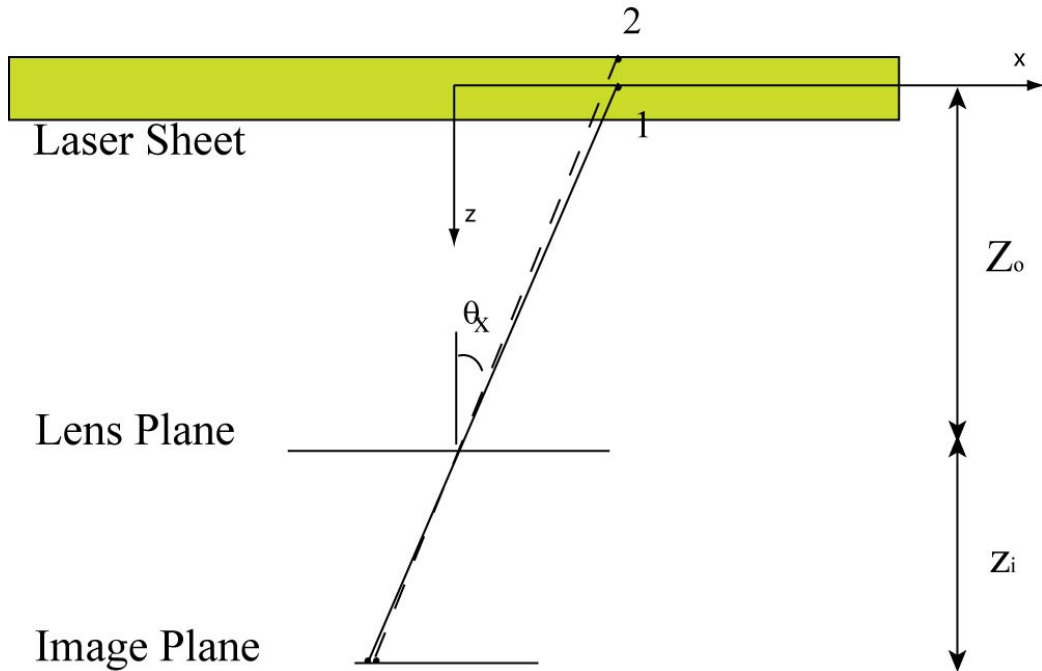
Fig. 3.1: A diagram of the laser sheet and camera lens positions.

With the magnification uncertainty, one can derive its impact on velocity. Since the velocity is only changed by the variation in magnification, its uncertainty is the same as the magnification uncertainty, which is proportional to $\Delta z_0 / Z_0$ [1]. So, to obtain an accurate quantification of the magnification uncertainty, the laser sheet thickness should be measured (if nothing else, to at least confirm that the magnification uncertainty is small).

3.2   Calibration

An important step that determines the success of PIV is the calibration of the camera. The camera acquires images in pixel dimensions, meaning it reports an intensity for each

6.45 μm square pixel on the imaging chip. These pixel dimensions need to be converted to a physical dimension (usually millimeters) for the velocity computation to be meaningful. For 2-component PIV, a ruler is often inserted on the laser plane to determine the scale of the image. The software then knows how many pixels are in a millimeter of physical space. For 3-component PIV, a 2 plane calibration plate is required.

When using a ruler, the user must be able to click two precise locations that are a known distance apart on a computer screen. For instance, the left edge of the lines on a ruler that are 1 in. apart. However, the camera does not have an infinite resolution, and the ruler line edge is usually smeared over several pixels. This smearing makes it difficult to determine exactly where the edge of the line is. This creates uncertainty on the calibration scale that could be significant.
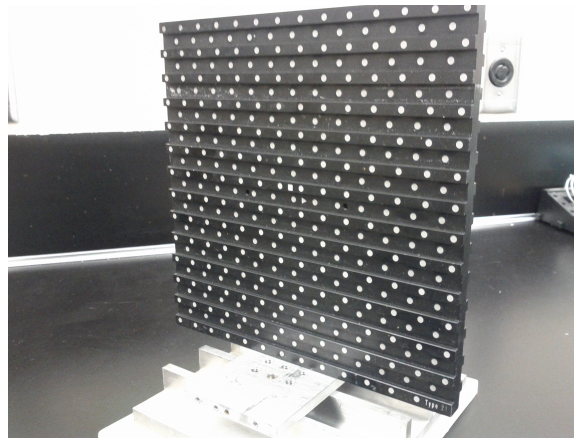
Fig. 3.2: A photograph of the Type 21 calibration plate.

A ruler calibration was repeated several times with different users and somewhat different situations (slight rotation off plane, sloppy pixel clicking). Variation in the calibration scales are used to find the error. The ruler calibration scale was also compared with the calibration scale that results from using the calibration plate, shown in Fig 3.2. It is assumed that the plate calibration does not have the errors that are inherently caused by the user when using a ruler calibration.

3.3 Perspective Error

Perspective error is caused by the angle of the viewing window. This is most significant when the viewing angle is wide and the particles undergo out of plane motion. Out of plane motion is when the flow is moving in a direction normal to the laser sheet. At wide viewing angles, out of plane motion appears as in plane motion and creates artificial velocity in the in-plane direction. Fig. 3.1 shows an example of the angle of a particle. It can be seen that motion out of plane (in the z direction) will change the perceived position of the particle.

To compute the error associated with out of plane motion and perspective, Prasad's equation [14] is used, which is $\epsilon = \left(\frac{\Delta z}{\Delta x} tan\theta_x, \frac{\Delta z}{\Delta y} tan\theta_y \right)$. The perspective error is a relative error between the true displacement on the object plane and the apparent in-plane displacement. In Prasad's equation, ϵ is the relative error due to perspective, Δz is the out of plane displacement, Δx and Δy are in plane displacements, and θ_x and θ_y are the respective angles for a position in the field of view (referenced from center).

The errors are based on the displacement of the particles at a specific point in the image. The perspective error can be computed with inputs of all three components of displacement and the position of a particle. To find the out of plane component of the displacement, another measurement was used where the laser fired spanwise across the jet, with the laser sheet plane in the jet. The camera looked down onto the jet. This out of plane measurement measured the u and w components of the velocity. Using this data, the isotropic turbulence assumption was confirmed (v' is the same as w'). In this jet, u' was 5% of u, and v' and w' were 3.7% of u.

Fig. 3.3 shows an example of the perspective error. The perspective error is usually highest in the corners of the imaging window. The center of the image should have zero perspective error, as is shown in Fig. 3.3.

An experiment was conducted to compute this uncertainty and included acquiring PIV data at two positions. A velocity profile was acquired in the center of the image at the first position. The second position viewing window was moved enough downstream to put the center of the first position at a location in the second window that should have elevated
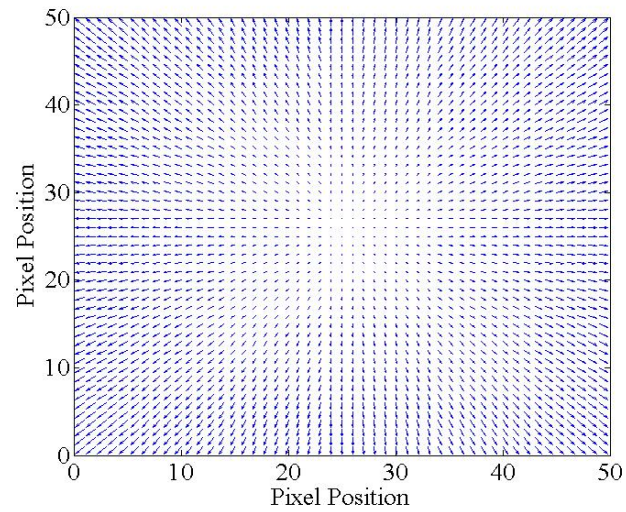
Fig. 3.3: An example of the perspective error field with uniform displacements in x, y and z.
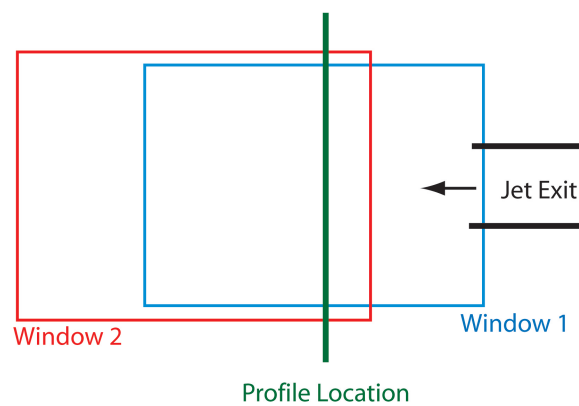
Fig. 3.4: A diagram of the two imaging windows with the velocity profile position. This was used to measure any significant perspective error.

perspective error. This setup is shown by Fig. 3.4. The two windows were of identical magnifications (the red and blue windows are of different size for display purposes only). The camera was simply moved downstream, parallel to the jet, with the same location from the jet exit in view in both windows.

3.4   Resolution

When acquiring PIV data, the scale of turbulence that can be resolved depends on the magnification of the camera. When the camera is zoomed in close to the laser sheet, smaller–scale fluctuations can be resolved. For example, a 32×32 pixel interrogation region covers a 0.25 mm^2 region when zoomed in, but only 2 mm^2 when the camera is further from the laser sheet. The zoomed in case covers a smaller physical region in space and can therefore resolve smaller–scale turbulence.

To quantify this error, several PIV data sets were acquired at various zoom levels. A zoomed in case, a middle range case, and a far back case. The magnifications are later referred to using their respective physical interrogation region size. The profiles and fluctuation levels were compared and the results are discussed in Chapter 4.

3.5   Algorithm

The cross-correlation algorithm used in DaVis software creates another source of uncertainty. The random artificial velocity level that is introduced from the algorithm is called noise. The algorithm noise is a function of several optical parameters, including particle image diameter and particle image density. This noise can be determined using a set of PIV data (1000 images from a jet for this case). The data uses double-frame images with a very small time difference (practically 0 μs). For the image shifting, only the first image was used (so the images correlated were identical, except for the shift). Fig. 3.5 shows raw PIV images for several particle diameters. The particle diameter d_τ is computed by fitting the correlation peak with a Gaussian and using Eq. 3.2, where σ is the standard deviation of the correlation fit.
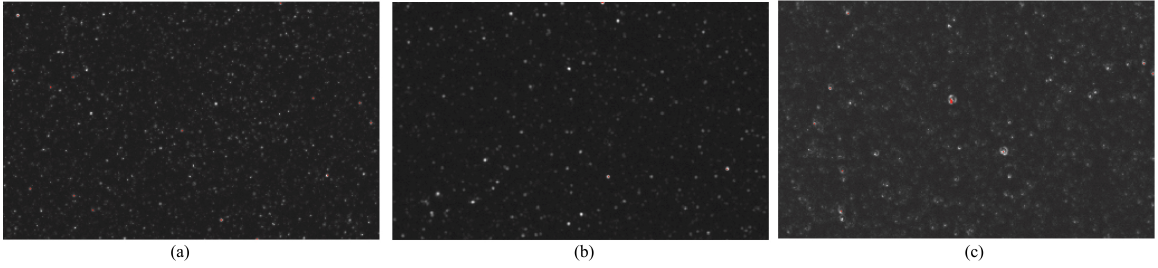
Fig. 3.5: Raw images for several particle diameters. (a) is 2.4 pixels, (b) is 3.8 pixels and (c) is 7.29 pixels.

$$d_\tau = 2\sqrt{2}\sigma \tag{3.2}$$

For the algorithm noise level, the first frame of each image is shifted a prescribed number of pixels. Then, the DaVis software computes the correlation and displacement field using the frame 1 and shifted frame 1 data set. Since the shift is a known value, the difference between the DaVis calculated and the known shift displacements are found.

A Matlab code was written to perform sub-pixel displacement following the outline shown in [15]. The starting image is a numerical grid of intensities (each cell representing one pixel). The grid is then interpolated to a refined grid. The refined grid was limited by both computer memory and the the desired sub-pixel displacement. The shift in the circshift subroutine (Matlab intrinsic) had to be an integer value, so the grid had to be refined enough to meet that requirement. This refinement was up to 10 times the original grid (meaning one cell became 100 cells on the fine grid). The fine image was then shifted a desired sub-pixel amount. Then the image was interpolated back to the original grid size. The original image and the shifted image were then correlated and compared.

The Matlab functions used in [15] include interp2 for the interpolation between grids and circshift for shifting on the fine grid. Another method was developed that was intended to help not smear the interpolation (which will be discussed more in the Results section). This second method sent the original image down to the fine grid, instead of interpolating it down. Then circshift was used to shift the fine gird image a specified amount. The mean

of the several pixels on the fine grid that make up one pixel on the coarse grid is then used to put the image back to the original grid size.

The expected displacement is an input to the analysis code. The 2 dimensional array of displacements computed with the DaVis code are compared to the expected displacement constant. A 2 dimensional array containing the difference between the two is reported. The maximum difference and the mean difference are computed, as well as uncertainty based on the random noise in the images.

The uncertainty of velocity is directly proportional to the uncertainty of the displacement. So, using a 95% confidence interval, the standard deviation of the difference between the input shift and the computed shift yields the uncertainty, that is, $1.96S_x$. Several factors are included in this uncertainty, including sub-pixel estimator, particle diameter effects, and intensity effects. Enough vectors from the images were used to converge the statistics.

Chapter 4

Results

Included are the results from the experiments and analysis discussed previously. The results are presented in the same order as previously presented.

4.1   Magnification

Several laser sheet profiles are shown in Fig 4.1. The Initial Volt trace in Fig. 4.1 is an initial intensity profile of the laser sheet, with an arbitrary pinhole diameter and shutter spacing. Small Space is a profile with the shutters spacing cut in half. The No Pin Volt trace is the laser intensity profile without the pinhole and with the shutters at the original spacing.
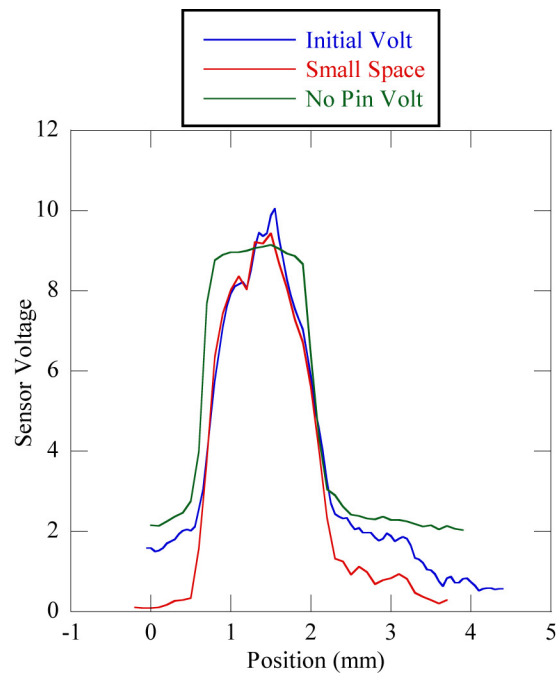
Fig. 4.1: The intensity profile of the high speed laser sheet.

It is shown in Fig. 4.1 that the smaller space between the shutters decreases the noise

amplitude in the laser sheet fringes (fringes likely caused by light refraction). The profile with no pinhole is closer to a step function than a Gaussian intensity profile. This shows that without the pinhole, the profile is spatially averaged. This averaging does not affect the calculated width of the laser sheet profile when using the positions of the profile at half of the maximum amplitude for the width. For the profiles in Fig. 4.1, the width is 1.5 mm.

A better computation for measuring the width is to use a 95% interval for the measurement. The high speed laser was focused for a different experiment and the profile was acquired using the photo-transistor. The width using 95% of the laser profile points was 0.7 mm. Fig. 4.2 shows the intensity profile for the refocused high speed laser.
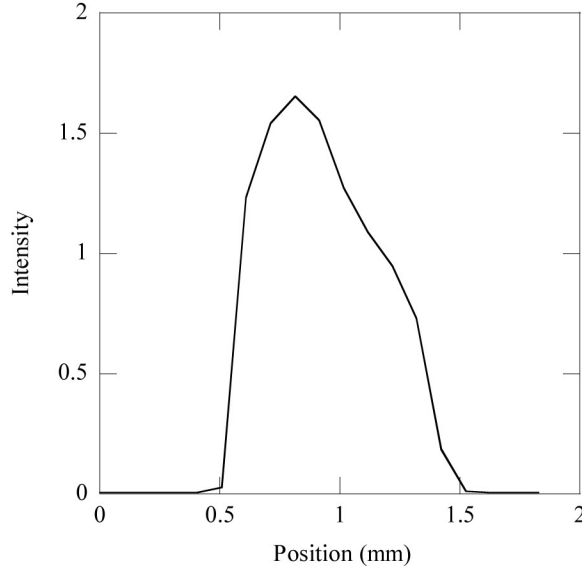
Fig. 4.2: Second intensity profile of the high speed laser sheet.

The variation of the velocity due to the variation of the magnification was computed for several laser sheet thicknesses. For a 3-mm thick laser sheet (too thick for most two-component PIV measurements), the velocity uncertainty can be as high as 0.4% for the velocity in the center of the laser sheet when the laser sheet thickness is 0.4% of the distance from the lens to the laser sheet plane (Z_0). So, the error of velocity due to the magnification change in the laser sheet is the same as the ratio of the laser sheet thickness to the object distance, $\Delta z_0/Z_0$ [1]. For the same setup where the object distance is 5 times smaller, the error would be 2%.

4.2 Calibration

By performing calibrations using a ruler versus a calibration target, the scaling factors for each can be compared. These factors are directly proportional to velocity, so relative error in the scaling factor is the relative error in the velocity (due to calibration only). The scaling factor from the calibration plate was compared with the ruler scaling factor for the similar calibration situations (such as a non-perpendicular calibration plate and ruler or an alignment that is as perpendicular as is possible).

In the first experiment, two different users calibrated the PIV system. The % column in Table 4.1 is the relative difference between the Best Estimate calibration scale and the respective case calibration scale. The scale factor is reported in mm/pixel. The Best Estimate scale factor was found by taking an average of the User 1, User 2 and User 2 Horizontal calibrations. The Area % column shows the percent of the image width that was used in the calibration.

Table 4.1: The calibration scale difference between two different users. User 2 calibrations were compared with User 1, who was more experienced. The difference is reported as a percent relative difference. The width of the image used in the calibration compared to the entire image width is reported as the Area %.

Description	Scale Factor	% Difference	Area %
Best Estimate	0.0426195	NA	NA
User 1	0.0426395	-0.04	94.7
User 2	0.0426493	0.07	94.6
User 2 Horizontal	0.0425698	0.12	87.5
User 2 Sloppy	0.0425932	0.06	94.7

In Table 4.1, User 1 is most experienced while User 2 has some experience (first year grad student). The User 2 Horizontal case was a calibration from User 2 with the calibration assuming the ruler is horizontal when the ruler was not horizontal. The User 2 sloppy was a fast calibration with the alignment of the ruler and camera not fixed to perpendicular angles (the alignment was just quickly eyeballed).

The two users had both used the software previously and User 1 has several years of experience with PIV experiments and calibration. As shown in Table 4.1, the difference in

calibration between two users and the Best Estimate is small. These results show that the calibration error of the user when using a ruler to calibrate is insignificant, so long as the user follows best practices. However, a small elevation in error results when an assumption is made incorrectly about the alignment of the image (which thus decreased the usable area of the calibration image). The error is still small, but shows that best practices should always be followed to keep this error in the range of insignificance.

Also considered is the difference in calibration scales between a ruler calibration and a plate calibration. First, the calibration plate was aligned with the camera to achieve the best possible calibration (meaning the plate is perpendicular to the camera imaging chip). Using DaVis 7.2 with its calibration scheme for the Type 21 calibration plate, a scale factor was obtained.

With the calibration plate aligned, a small ruler was fixed to the front of the plate (so the camera would see the ruler, not the plate). The camera was moved back the distance of the thickness of the ruler to match the field of view dimensions with the plate calibration. Then a calibration scale was obtained using the ruler method. Table 4.2 shows the difference between the plate and ruler calibrations. The scale factor is reported in mm/pixel and the percent relative difference column is simply the difference of the plate and ruler scale factors for the specific setup (the rotated cases were compared with each other and the non-rotated calibrations were compared with each other). The ruler calibration is treated as the best estimate in both the rotated and non-rotated cases.

Table 4.2: The calibration scale difference between the ruler and plate calibrations. The % column is reported as a percent relative difference between the ruler and plate calibration. The non-rotated cases were compared with each other, and the rotated cases were compared with each other.

Description	Scale Factor	% Difference	Area %
Ruler	0.0451015	NA	89.3
Plate	0.0450840	0.04	81.3
Ruler Rotated	0.0453958	NA	95.7
Plate Rotated	0.0454681	0.16	80.9

Table 4.2 shows that the difference in the calibration scale between a ruler and plate

calibration is small for a perpendicular setup. The difference increases when the plate and ruler are rotated 4°, which is noticeably misaligned (a normal user would have a closer to perpendicular alignment than the 4° rotation). The plate calibration corrects for the warping of the image when it is rotated. However, both differences are still insignificant.

The previous experiments were performed with a 50-mm lens. Subsequently, the lens was replaced with a 28-mm lens. The results for the plate and ruler comparison using the wider angle lens (28 mm) are shown in Table 4.3.

Table 4.3: The calibration scale difference between the ruler and plate calibrations for a 28-mm lens. The % column is reported as a percent relative difference.

Description	Scale Factor	% Difference	Area %
Ruler	0.085182	NA	85.4
Plate	0.08508538	0.11	94.6

Table 4.3 shows that the difference between the plate and the ruler calibration for the wide angle lens is higher than for the 50-mm lens. This shows that there exists an increase in calibration error when the field of view is wide and/or the angle of the calibration source (a ruler) is not perpendicular. However, the increased uncertainty is still quite insignificant for these situations.

For a trained user following best practices, the error resulting from calibration is insignificant for 2-component calibration using either a ruler or a calibration plate.

4.3 Perspective Error

Using the equation for perspective error, the expected perspective error field was computed for a given experimental setup as a function of position in the field of view and the through-plane component of velocity. A code was developed to compute this error and was checked with the results in [1]. Recall that the flow that was tested has a zero mean component of velocity normal to the measurement plane. Therefore, the bias error from perspective is also zero. However, turbulent fluctuations normal to the measurement plane will add to the measured fluctuations of the other two velocity components.

For the experimental setup conducted in this work, the maximum computed perspective error (which is at the corners of the image) was always small. This was confirmed with experimental data for the jet experiment. As an example, the experimental setup used for Window 1 in Fig. 4.3 was used to calculate the expected perspective error. Using the perspective error equation, the maximum perspective error was found to be less than 0.2×10^{-6} m/s. For this comparison, the θ_x in Fig. 3.4 was $1.1°$ at the widest angle. The laser sheet was 1.5 mm and z_0 was 43.18 cm and the turbulence was assumed to be isotropic (fluctuations in v and w were the same).
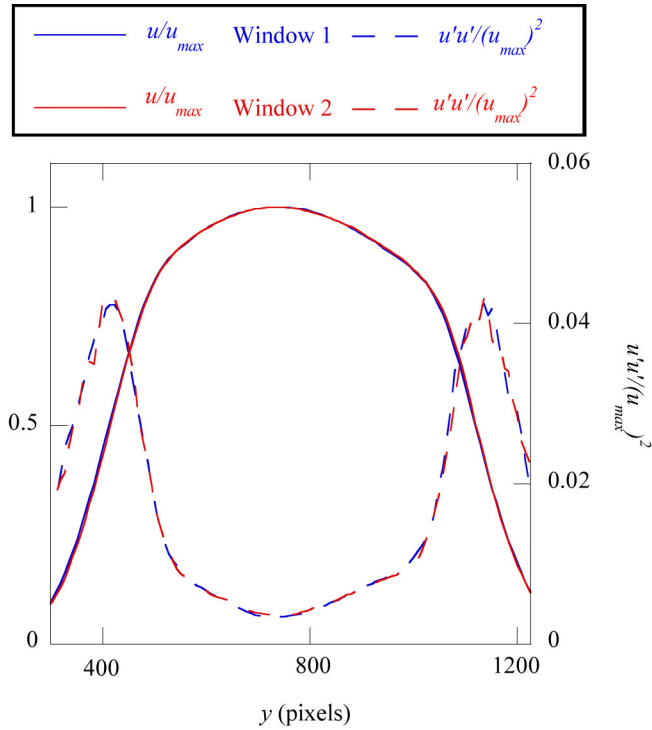
Fig. 4.3: The normalized velocity and fluctuation profiles for the two windows shown in Fig. 3.4.

Fig. 4.3 shows the velocity profile normalized by the maximum velocity for the two viewing windows, and the fluctuations in the velocity (normalized by the same maximum velocity). The fluctuations in Fig. 4.3 were computed in DaVis 7.2 (reported as the RMS in that software). The fluctuations were normalized by the peak of the velocity profile. The high fluctuations in the Window 2 case are from seeding.

From Fig. 4.3, it is found that the perspective of the viewing window has no significant impact on the velocity profile for this experimental setup. This is not true for every experiment, as a wider angle lens will have a larger perspective error (these data were acquired using a 105-mm lens). Images at a high magnification will also have elevated perspective error. For each experiment, the perspective error field should be computed. If possible, experimental confirmation of the computed perspective error should also be performed.

4.4   Resolution

The turbulence scales that can be resolved can impact the velocity fluctuation level of the PIV result. PIV data for three different magnifications were acquired. All three data sets contained the profile location that is investigated. The velocity profiles for the three magnifications are shown in Fig. 4.4. The mean velocity is nearly identical for the three cases (as expected), but the fluctuation levels increase as the field of view becomes smaller, particularly in regions of large shear. It seems that in these regions, a significant number of turbulent eddies have become larger than the interrogation region for the largest field of view. This leads to averaging the velocity in space and an attenuation of the measured fluctuations. In Fig. 4.4, the number of the different magnifications in the legend represent the physical size of an interrogation region in millimeters. The jet height was 12.7 mm.

Fig. 4.5 shows the Fourier transform of a hot wire sample in time at the fluctuation peak of the jet, along with three PIV samples across an image with the sample taken along the fluctuation peak of the jet. Using Taylor's Frozen Turbulence hypothesis, the spatial and temporal frequencies can be compared. The hot wire frequency was converted to 1/m using the average velocity in the sample. Fig. 4.5 also shows the length of the hot wire sensing wire, HWA, and the laser sheet thickness, LST.

The interrogation regions are squares when viewed from the camera. However, realistically, each region is a rectangular volume with the third dimension being the thickness of the laser sheet. In 2-component PIV, the third dimension that is not measurable adds uncertainty to the overall PIV measurement (which is included in the magnification and perspective errors). The interrogation volume can also attenuate the measured turbulence
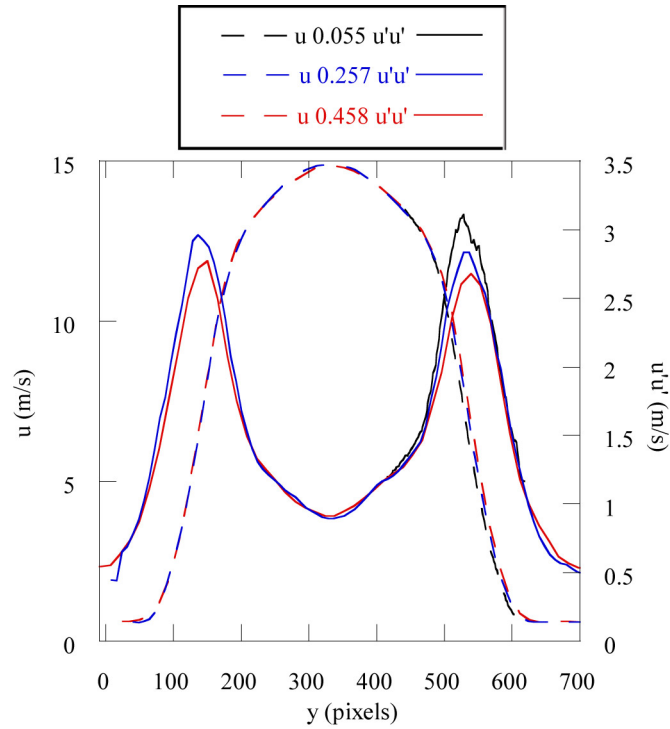
Fig. 4.4: The velocity and fluctuation profiles for the three different zoom levels. The Close case has only half of the jet visible in the imaging window.
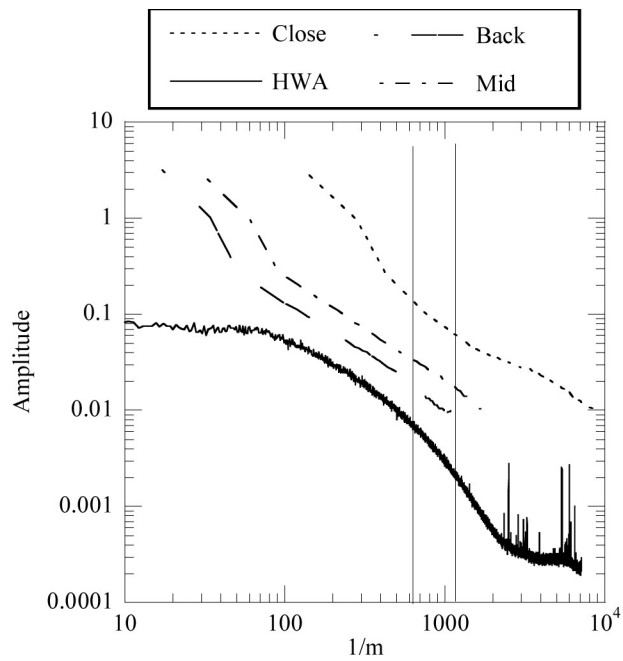

Fig. 4.5: The Fourier transforms of hot wire data and three magnifications of PIV data on the jet fluctuation peak. LST represents the laser sheet thickness and HWA represents the width of the hot wire sensor.

fluctuations.

The PIV data in Fig. 4.5 does not provide enough information to make conclusions because of the size of the interrogation regions with respect to the laser sheet thickness. Fig. 4.6 shows the laser sheet thickness and the relative size of one interrogation region for each magnification. The Close interrogation region is so small in the in-plane direction that it should see the smallest scale fluctuations of the three magnifications. However, it is so deep in the out of plane direction that it includes larger scale out of plane fluctuations, thus averaging the measured fluctuations. The smallest interrogation region size should only see the small scale fluctuations, so these magnifications are not useful.
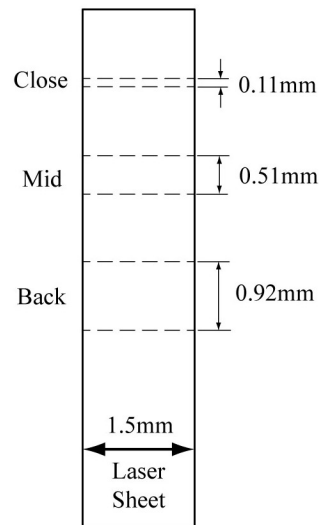
Fig. 4.6: Sketch of the laser sheet thickness and the interrogation region sizes for the three different magnifications (scaled relative to the laser sheet thickness).

The magnification of the images and the thickness of the laser sheet create too small of interrogation regions for this resolution study to be conclusive. The study would be better performed with a thinner laser sheet and corresponding magnifications with the smallest interrogation region being the same width as the laser sheet thickness. The other magnifications would then have a larger interrogation region size than the laser sheet thickness.

4.5   Algorithm

The "noise floor" is the best-case scenario random error and is the uncertainty of a measurement found from shifting an image a known displacement, computing the correlation, and then comparing the correlation to the known displacement. First, 1000 images were correlated with themselves and the noise level was computed. This is referred to as zero shift of the images. Then the images were shifted in the sub-pixel region and correlated.

4.5.1   Zero Shift

Fig. 4.7 shows raw particle images for two particle diameters. The smaller diameter image appears to have a better focus than the larger particle images.

(a)   (b)
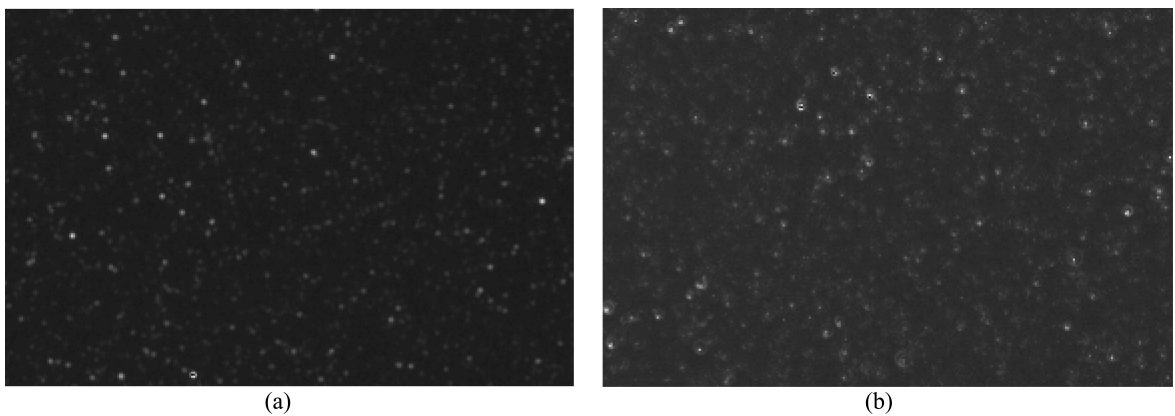
Fig. 4.7: Raw data for particle diameters of 3.8 (a) and 4.5 (b).

Fig. 4.8 shows the uncertainty for images with no shift, correlated with PRANA. All of the uncertainty values in Fig. 4.8 are small, though uncertainty tends to increase with particle image size. The noise floor found for zero shift images in PRANA is a base value that can be used for the uncertainty analysis of the images. It does not include the sub-pixel estimator, however. DaVis 7.2 reported zero displacement, identically, for zero shift images. Conversations with LaVision seem to indicate that DaVis attempts to detect this condition and reports 0 displacement. Therefore, this test cannot be performed with DaVis.
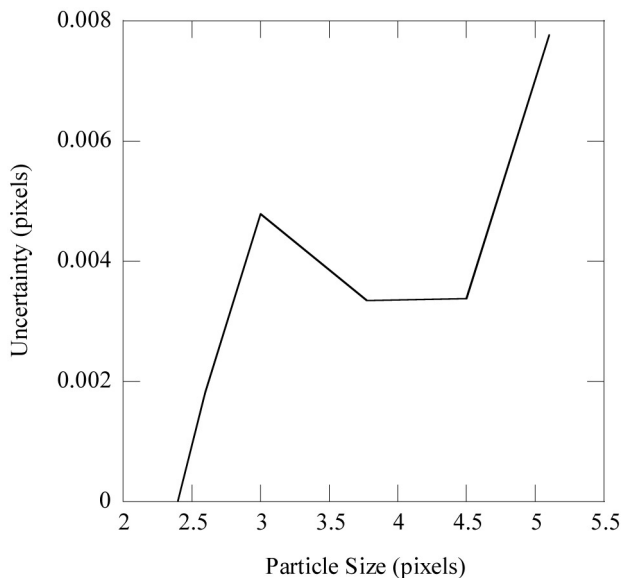
Fig. 4.8: Uncertainty floor for no shift images correlated with PRANA.

4.5.2 Shifted Images

The images were then shifted using the method described in [15]. Several different cases with different particle image diameters were used.

When images are shifted, the intensity of the images spread through the surrounding pixels. Fig. 4.9 shows the particle images for a shift of 0.5 pixels with a particle diameter of the original image of 2.4 pixels (near optimal, according to Raffel [2]). The smearing of the particles is obvious.

(a)   (b)

Fig. 4.9: Raw images for particle diameter of 2.4 pixels. (a) shows the original image and (b) shows the 0.5 pixel shifted image.

Fig. 4.10 shows the particle images for sub-pixel displacement with a particle image diameter of 7.3 pixels. Fig. 4.10a shows the original image and (b) shows the shifted image. The shifting algorithm is the same as that used in Fig. 4.9, but the particles are larger. On inspection, the images look nearly the same. The small particles create larger spatial frequencies than the larger particles, and the high frequencies are smeared to lower frequency due to the upsampling procedure.

(a) (b)

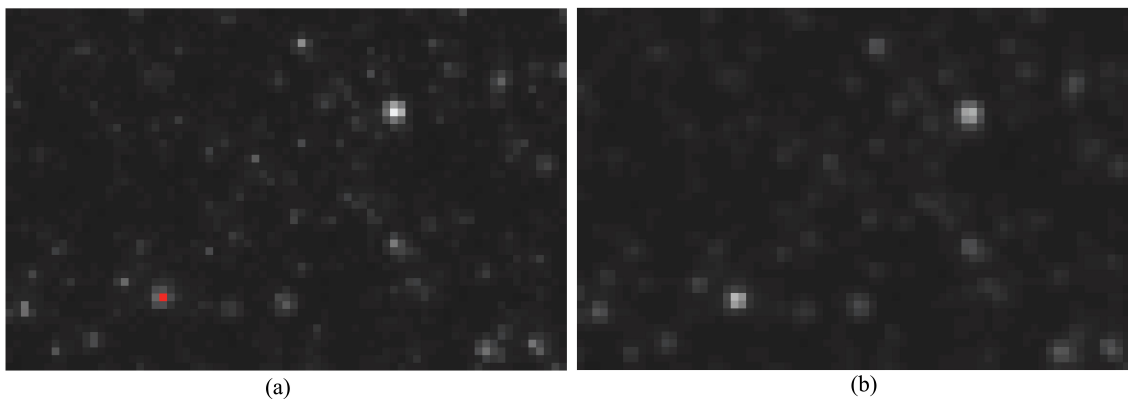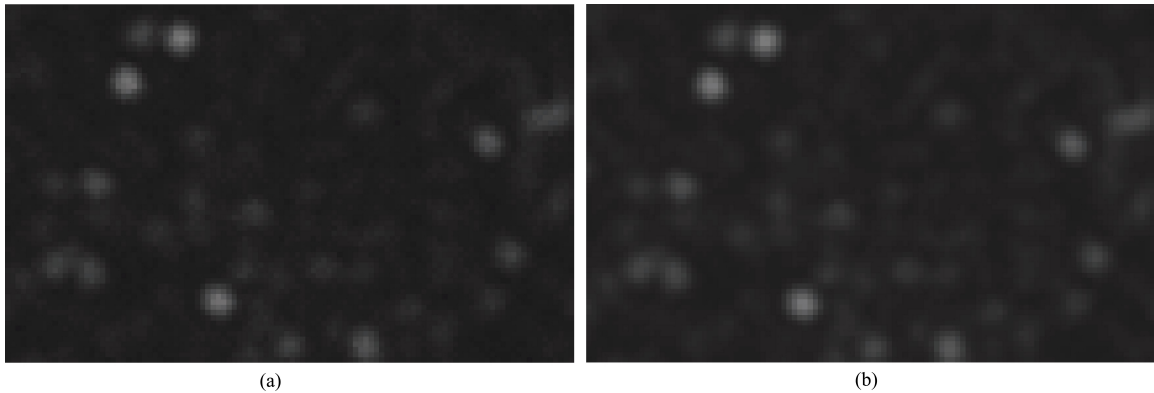Fig. 4.10: Raw images for particle diameter of 7.3 pixels. (a) shows the original image and (b) shows the 0.5 pixel shifted image.

The scheme used in [15] tends to smear particles when shifting images with optimal particle diameters (like the data in Fig. 4.9). This voids the validity of using shifted images to compute a noise floor.

To quantify the smearing of the image shifting, spacial Fourier transforms were computed on the image. A low frequency would mean that the particles intensity is smeared or averaged over several pixels. A high frequency shows sharp peaks of intensity (or well focused particles). Fig. 4.11 shows the Fourier transform (FFT) of the images in the data set shown by Fig. 4.9.

Fig. 4.11 shows the Fourier transform across an image that was shifted 0.6 pixels. The First trace is from the original image, and the Second is from the shifted image. As is shown, the high frequencies that exist in the original image are attenuated in the second, shifted image. For small particles where the particle is only a few pixels large, this smearing drastically changes the particle shape. For a large particle where the original particle image

Fig. 4.11: The Fourier transform across the horizontal direction of the raw particle image for the original image and the shifted image. This case was shifted 0.6 pixels in both horizontal and vertical directions. This case had a particle diameter of 2.4 pixels.

was made up of many pixels, this change in shared pixels doesn't change the particle shape significantly.

Fig. 4.12 shows the FFT of an image with large a large particle diameters (the data shown in Fig. 4.10). The smearing is non-existent for this particle size, as shown by the high frequency being equally present in both images.

Shifting the image diagonally was obviously smearing the image, so a uni-directional shift was implemented to see if this helped decrease the smearing. Fig. 4.13 shows the Fourier transform in the direction perpendicular to the image shift. This FFT is practically the same as the original image, as expected. No smearing occurred in the direction opposite the shift.

Fig. 4.14 shows the FFT in the direction of the shift compared with the FFT of the original image. Again, smearing is shown by the decreased high frequencies. The algorithm is smearing the particle images over several pixels, even when the shift is only done in one direction instead of two.
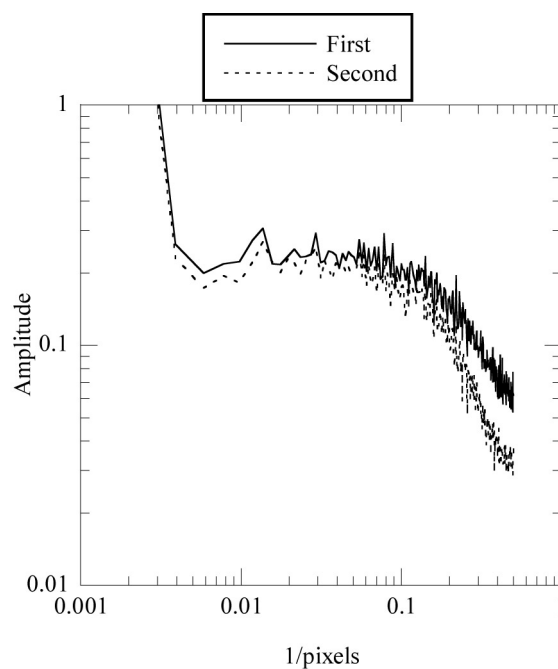
Fig. 4.12: The Fourier transform across the horizontal direction of the raw particle image for the original image and the shifted image. This data was shifted 0.6 pixels in both horizontal and vertical directions. This data had a particle diameter of 7.3 pixels.

Fig. 4.13: The Fourier transform across the horizontal direction of the raw particle image for the original image and the shifted image. The profile for this set was taken horizontally across the image with the shifted image being shifted in the vertical direction.
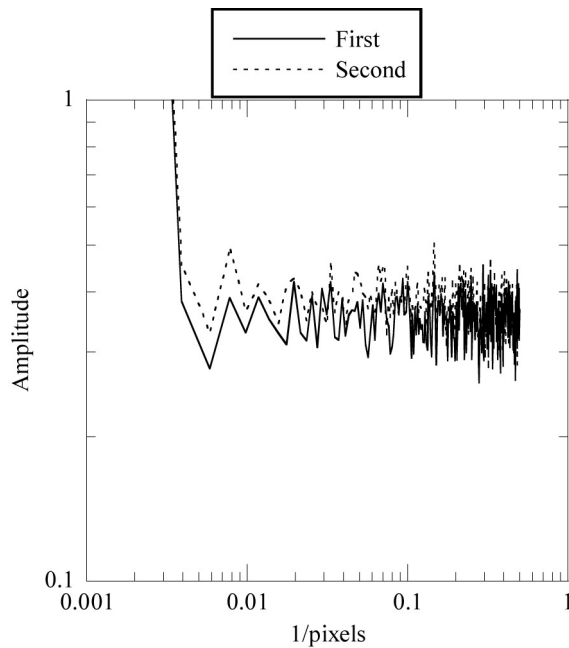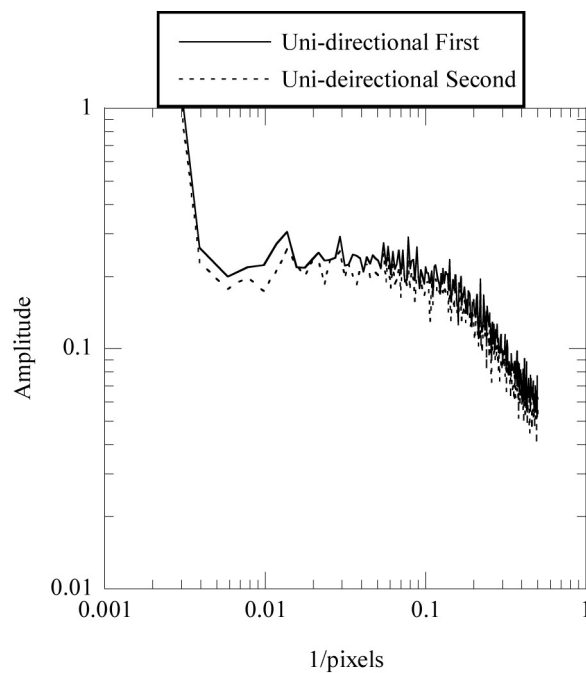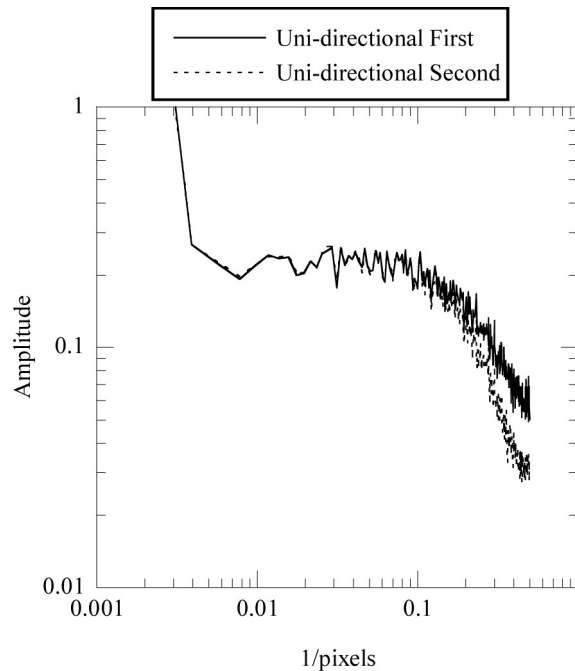
Fig. 4.14: The Fourier transform across the horizontal direction of the raw particle image for the original image and the shifted image. The profile for this set was taken vertically across the image with the shifted image being shifted in the vertical direction.

Fig. 4.15 shows the uncertainty (in pixels) for sub-pixel displacements using clear (or well focused) data (particle diameter of 2.1 pixels) and blurry data (particle diameter of 5.6 pixels). The data is comparable to that shown in Fig. 4.7. Fig. 4.15 shows that the large particle diameter has lower uncertainty than the small particle diameter. This is opposite of what has been shown in other studies [2], and these trends are likely due to the smearing effect.

Since the uncertainty is a function of the particle diameter, several different particle image diameters were compared. Fig. 4.16 shows the uncertainty as a function of particle displacement for seven particle diameters. For small sub-pixel displacement and near 1 sub-pixel displacement, the uncertainty is smaller than in the mid-range sub-pixel displacement. The trend in Fig. 4.16 for any single case is expected due to peak-locking. However, the trend with particle image diameter is incorrect due to the shifting scheme.

A Fourier transform of data taken across an image can show the extent of smearing in the image shifting. For sharp particle images, the FFT will yield more high frequencies
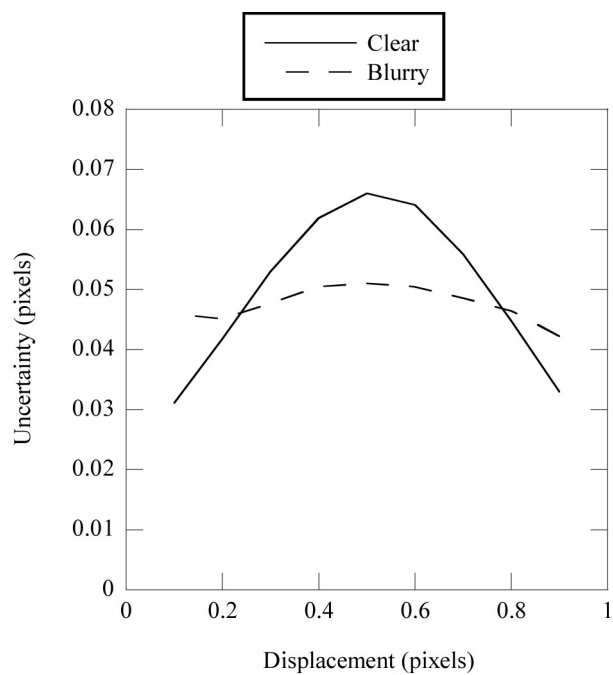
Fig. 4.15: Uncertainty in the x-displacement for sub-pixel displacement for two different data sets. Clear has a particle diameter of 2.1 pixels, and Blurry has a particle diameter of 5.6 pixels.

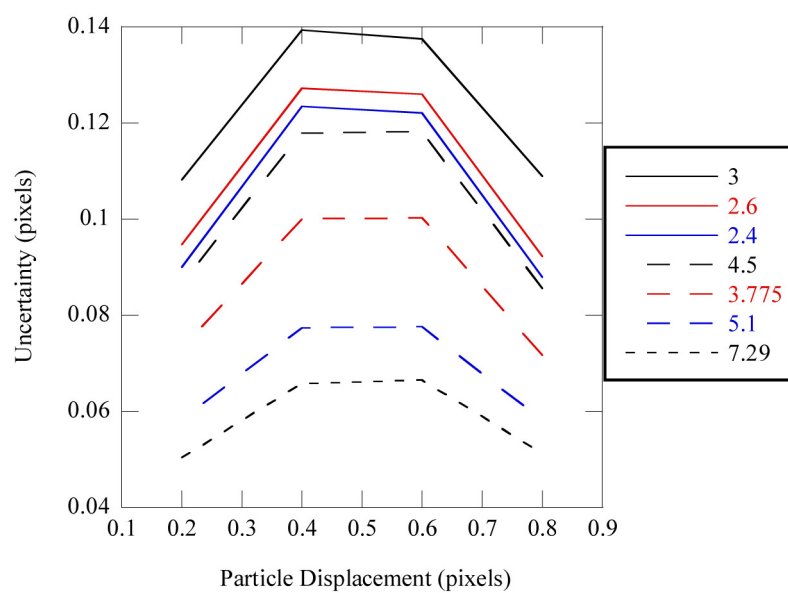
Fig. 4.16: Uncertainty in the x-displacement for sub-pixel particle displacement for several particle diameters. Correlation computed using DaVis7.2.

than a blurry or smeared image of the particles. Since the particle diameters are being changed as the image is shifted, the shifting algorithm outlined in [15] requires adjustment before being used on data with optimal particle image diameters.

Chapter 5

Conclusions

The magnification error is usually negligible for most PIV experiments. However, this error can be significant if the laser sheet is too thick. The laser sheet thickness should be measured and properly focused for each specific experiment.

The error on the velocity from the calibration is generally insignificant, so long as best practices are followed. If two trained students calibrate using a ruler calibration source, the difference in the scale factor (and therefore, velocity) is small. If some wrong assumptions are made in the calibration, the difference between calibrations increases, but is still small. Also, the difference between calibrations using the calibration plate and a ruler is small. There is an increase in calibration error when the calibration source is rotated or if a wider field of view lens is used.

The error introduced from the camera perspective was found to be insignificant for this experimental setup. An example is presented to confirm the insignificance of the error by using two different viewing windows and a velocity profile in both. The profile in one is expected to have small perspective error, and the other is expected to have elevated perspective error. The expected perspective error field can also be computed using the experimental setup parameters (camera distance, laser sheet thickness).

The uncertainty from turbulence resolution should be analyzed. As can be seen, as one zooms in on the jet for this experiment, more turbulence is resolved. Care must be taken to keep the laser sheet thickness thinner than the width of the smallest interrogation region. When out of plane fluctuations appear as in plane fluctuations, the turbulence scale resolution is not reliable.

The uncertainty that comes from using a correlation algorithm is called a noise floor. The uncertainty from this algorithm noise should be quantified and is a function of several

optical parameters, including particle density and particle diameter. A slightly out of focus (5.6 pixel particle diameter) image creates a less uncertain sub-pixel noise floor than an in focus data set (2 pixel particle diameter), using the methods described herein. Large particle diameters should have higher uncertainty than small particle diameters, so a different method should be developed for small particle sizes. This noise floor is different for every algorithm (such as DaVis 7.2 and PRANA), and should be computed for an experiment. For a zero shift displacement, DaVis 7.2 cannot provide correlation data for the noise floor.

References

[1] Adrian, R. J., and Westerweel, J., 2011. *Particle Image Velocimetry*, Vol. I. Cambridge University Press, New York.

[2] Raffel, M., Willert, C., and Kompenhans, J., 1998. *Particle Image Velocimetry*. Springer-Verlag, Berlin Heidelberg.

[3] pivonline, 2012. Particle image velocimetry uncertainty workshop. `http://www.piv-online.org/PIVUWS/PIV_Uncertainty_Workshop/PIV_Uncertainty_Workshop.html`.

[4] Willert, C., and Gharib, M., 1991. "Digital particle image velocimetry.". *Experiments in Fluids,* **10**(4), pp. 181–193.

[5] Nishino, K., Kasagi, N., and Hirata, M., 1989. "Three-dimensional particle tracking velocimetry based on automated digital image processing." *ASME J Fluids Eng,* **111**(4), pp. 384–391.

[6] Prasad, A. K., Adrian, R., Landreth, C., and Offutt, P., 1992. "Effect of resolution on the speed and accuracy of particle image velocimetry interrogation." *Experiments in Fluids,* **13**, pp. 105–116.

[7] Keane, R., and Adrian, R., 1992. "Theory of cross-correlation analysis of piv images.". *Applied Scientific Research,* **49**(3), JUL, pp. 191–215.

[8] Adrian, R. J., 2005. "Twenty years of particle image velocimetry." *Experiments in Fluids,* **39**(2), pp. 159 – 169.

[9] Bolinder, J., 1999. On the accuracy of a digital particle image velocimetry system. Tech. rep., Lund Institute of Technology.

[10] Nogueira, J., Lecuona, A., and Rodriguez, P., 1997. "Data validation, false vectors, correction and derived magnitudes calculation on piv data." *Measurement Science Technology,* **8**, pp. 1493 – 1501.

[11] Westerweel, J., 1994. "Efficient detection of spurious vectors in particle image velocimetry data." *Experiments in Fluids,* **16**, pp. 236 – 247.

[12] ASME, 2008. ANSI standard V&V 20. ASME guide on verification and validation in computational dynamics and heat transfer.

[13] Coleman, H. W., and Steele, W. G., 2009. *Experimentation, Validation, and Uncertainty Analysis for Engineers*. John Wiley & Sons, Inc.

[14] Prasad, A. K., 2000. "Stereoscopic particle image velocimetry." *Experiments in Fluids,* **29**, pp. 103–116. 10.1007/s003480000143.

[15] McPhail, M., Weldon, M., Krane, M., Fontaine, A., Petrie, H., Buchanan, J., Lorentz, D., and Bauer, R., 2011. "Practical estimation of DPIV uncertainty using pseudo-image pairs.". 64th Annual Meeting of the APS Division of Fluid Dynamics.

Appendices

Appendix A

Code for Noise Floor Calculation

This code was written in Matlab R2010b. This routine simply reads an IM7 image from DaVis, creates a refined grid, fills the grid with an interpolated version of the image, shifts the image a desired number of pixels in non-refined grid dimensions, then interpolates back to the original grid size providing a shifted image with possible sub-pixel displacement.

```
clc; clear all; close all


% Open the particle Image 1
Img1 = loadvec('BrandonsDatatest.IM7');


% Extract the position vectors from the Img1 structure.
X=Img1.x;
Y=Img1.y';


% Extract the intensity map from the image of particles.  Each value in
% this array corresponds to a pixel on the image chip.
I_map=Img1.w;
fprintf(['The max intensity in Image 1 is ', num2str(max(max(I_map))),'\n'])
fprintf(['The min intensity in Image 1 is ', num2str(min(min(I_map))),'\n','\n'])
imwrite(I_map./max(max(I_map)),'Image1.bmp','bmp');


% Use interp2 to refine the grid size.  In order to work, the spacial
% position vectors must be defined first.  The Y vector needed to be
% transposed to work the the interp2 function.
```

```
scale=4;


xstep=(X(2)-X(1))/scale;

X_new(1:size(X,2)*scale)=0;

X_new(1)=X(1)/scale;

for i=2:size(X,2)*scale

    X_new(i)=X_new(i-1)+xstep;

end


ystep=(Y(2)-Y(1))/scale;

Y_new(1:size(Y,1)*scale)=0;

Y_new=Y_new';

Y_new(1)=Y(1)/scale;

for i=2:size(Y,1)*scale

    Y_new(i)=Y_new(i-1)+ystep;

end


I_map_new=interp2(Y,X,I_map,Y_new,X_new);


% Now use circshift to create a new image that is shifted several pixels.

%  To shift an interpolated image on a 5X finer grid the equivalent of 0.6

%  pixels in the original image, the shift is 0.6/0.2 = 3 pixels (from

%  Petrie, PIV Workshop, 2011).

xshift=10*scale; %This will go 10 pixels in the original space

yshift=0;

I_map2_fine=circshift(I_map_new,[xshift,yshift]);


% Now interpolate back to the original grid size.
```

```
I_map2=interp2(Y_new,X_new,I_map2_fine,Y,X);


fprintf(['The max intensity in shifted Image 1 is ',..
 num2str(max(max(I_map2))),'\n'])
fprintf(['The min intensity in shifted Image 1 is ',..
 num2str(min(min(I_map2))),'\n','\n'])


I_map2(isnan(I_map2)) = 0;
% Write the two images as .IM7 for use in DaVis or Prana
imwrite(I_map2./max(max(I_map2)),'Image2.bmp','bmp');


fprintf(['Done! ','\n'])
```

Appendix B

TKE Computation code

This code was written in Fortran 95 and compiled with gfortran. It simply takes a vector field from DaVis, extracts a profile across the jet, and computes the turbulence kinetic energy using the isotropic turbulence approximation ($v' = w'$).

```fortran
Program tkecomputer
USE subs
Implicit none


REAL, DIMENSION(172) :: tke
REAL, DIMENSION(172) :: velocityx,velocityy,velocityz
INTEGER :: i,j
INTEGER,PARAMETER :: length=21


CHARACTER(len=length) :: filename
CHARACTER(len=length+7):: filename2


write(*,*) "Running ..."
filename='Average_uv\B00002.DAT'


CALL Davis_read2(length,filename,filename2)


filename2=filename//'_Vx.txt'


CALL vert_profex(length+7,trim(filename2),filename)
```

```fortran
CALL profilereads(filename2, 172, velocityx, length+7)


filename2=filename//'_Vy.txt'


CALL vert_profex(length+7,filename2,filename)


    ! for each file, read in the hotwire data
CALL profilereads(filename2, 172, velocityy, length+7)


velocityz=velocityy


OPEN (unit=99, file='TKE.txt')
DO i=1,172
tke(i)=0.5*(velocityx(i)**2+velocityy(i)**2+velocityz(i)**2)
write(99,*) i, tke(i)
END DO


close(99)


write(*,*) "Done with TKE!  Cheers"
write(*,*) "--------------------------------------------"
END PROGRAM



Subroutine Davis_read2(length,filename,filename2)!,Vx,Vstd)
!Puts a Davis .DAT file into an array format
implicit none
integer:: length, ierr
```

```fortran
character(len=length)::filename,filename2

character(len=length):: folder

character(len=length):: file1, file2

character(len=33):: dummy, heading3

character(len=12)::filepart

integer:: line_num, i, j, count

real, dimension(1:172,1:128):: Vs, Vstds,Vxx,Vyy

real, dimension(1:128*172):: x,y,Vx,Vy, Vstd, x2, y2!x,Vy


file1=filename


OPEN(unit=84, file=file1)!,status='old',IOSTAT=ierr)


read(84,*) dummy

read(84,*) dummy

read(84,*) heading3


line_num=128*172


do i=1,line_num

  read(84,*) x(i), y(i), Vx(i), Vy(i)

end do


 write(*,*) "Davis_read3.f95 has completed the file read"

 write(*,*) "Sorting to an array..."


count=0

do i=1,172
```

```
   do j=1,128

      count=count+1

      Vs(i,j)=sqrt((Vx(count)*Vx(count))+(Vy(count)*Vy(count)))

Vxx(i,j)=Vx(count)

Vyy(i,j)=Vy(count)

   end do

end do

file1=trim(file1)

OPEN(unit=85, file=file1//'_V.txt')

OPEN(unit=82, file=file1//'_Vx.txt')

OPEN(unit=83, file=file1//'_Vy.txt')


do i = 1,172

  write(85,*) Vs(i,:)

  write(82,*) Vxx(i,:)

  write(83,*) Vyy(i,:)

end do


 write(*,*) "File has been written.  End of Davis_read."

 write(*,*) file1//'_V.txt'

 write(*,*) ' '


close(79)

Close(85)

Close(84)

Close(82)

close(83)
```

```
End Subroutine



subroutine vert_profex(length,filename,filename2)
implicit none


integer:: length, i, proloc
character(len=length)::filename,filename2
character(len=length):: folder
character(len=length+15):: file1, file2


real, dimension(1:172,1:128):: Vs, Vstds


file1=filename!//"_V.txt"


open(unit=80, file=file1)


 write(*,*) '--------------------------------'
 write(*,*) 'Running vert_profex.f95 (the horizontal profile extractor)'
 write(*,*) 'File to be used are:'
 write(*,*) filename


do i = 1,172
  read(80,*) Vs(i,:)
end do


proloc=800! 588 532
```

```
close(80)


open (unit=101, file=filename//"Horiz_Profile.txt")


! 1020 pixels and 128 vectors in the horizontal direction, 8 pix/vector
proloc=(4.+proloc)/8.


do i=1,172
  write(101,*) Vs(i,proloc)
end do


close(101)
write(*,*) "Done with horiz_profex.f95!"
write(*,*)
end subroutine



subroutine profilereads(filename, samples, vel, length)
implicit none


! routine to read in the hot wire data sets, one file per call
! this routine sends the velocity back to the driver program
integer:: j, samples, ierr1, length
real, dimension(samples)::count
real, dimension(samples):: v, vel
character(len=length), intent(in):: filename


open(unit=99, file=filename//'Horiz_Profile.txt')!, iostat=ierr1)
```

```
do j=1,samples

  read(99,*) vel(j)

end do


close(99)

end subroutine
```